mater.scichina.com link.springer.com

Published online 14 October 2022 | https://doi.org/10.1007/s40843-022-2255-2
Sci China Mater 2022, 65(12): 3361–3367

SPECIAL ISSUE: Energy Transitions towards Carbon Neutrality

Anionic surfactant anchoring enables 23.4% efficient and stable perovskite solar cells

Tao Wang[1,2,3], Tianshi Ye[1,2,3], Liang Qiao[1,2,3], Weiyu Kong[1,2,3], Fang Zeng[4], Yao Zhang[1], Ruitian Sun[1,2,3], Lin Zhang[1,2,3], Han Chen[1], Rongkun Zheng[4] and Xudong Yang[1,2,3*]

ABSTRACT Nonradiative recombination losses at defects in metal halide perovskite films are responsible for hindering the improvement of the photovoltaic performance and stability of perovskite solar cells (PSCs). Here, we report a feasible multifunctional additive strategy that uses cesium stearate to passivate defects in perovskite films and simultaneously enhances the tolerance to light and moisture stress. Nonradiative recombination losses are effectively suppressed in target films that exhibit improved crystallinity, low trap-state density, and enhanced carrier separation and transportation. The present strategy hence boosts the power conversion efficiency of the p-i-n structured PSC to 23.41%. Our device also shows good stability in ambient air without encapsulation, maintaining 91.6% of the initial efficiency after 720 h.

Keywords: perovskite solar cells, cesium stearate, crystallization, passivation, stability

INTRODUCTION

Hybrid organic-inorganic metal halide perovskite solar cells (PSCs) have attracted considerable interest over the past decade due to their ever-increasing power conversion efficiency (PCE) and low fabrication cost, making PSCs a promising candidate for the next-generation photovoltaic technology [1–3]. Recently, inverted structural PSCs, with great advantages in operational stability and compatibility for perovskite-based tandem solar cells, have achieved PCEs >25% through different strategies, such as surface engineering [4–7]. However, presently recorded PCEs are still behind the Shockley-Queisser (SQ) radiative limit and have stability lags far behind those of commercial photovoltaic devices, such as crystalline silicon with 25-year commercial warranties [8,9]. To further enhance photovoltaic performances toward the SQ radiative limit and simultaneously improve the long-term stability of PSCs, nonradiative recombination losses should be minimized [8,10]. Defect-assisted recombination at surfaces and grain boundaries is the main source of nonradiative recombination losses [8]. Uncontrollable crystallization during the solution preparation makes trap defects inevitable [11]. Even worse, these defects provide pathways for ion migration and present fragile initiation sites for degradation by extrinsic stress, resulting in the decomposition of the perovskite structure [9,12]. Additive strategies have been widely utilized to passivate trap defects through coordination or ionic bonding, including metal salts (e.g., Cs^+ and K^+) [13–15], ammonium salts (e.g., octylammonium and phenylethylammonium) [16–19], Lewis acids (e.g., fullerene derivatives) [20–22], and Lewis bases (e.g., caffeine) [23–25]. However, the counter anions of metal and ammonium cations are mostly halide ions (chloride or iodide ions) that are light sensitive and prone to volatilize and migrate, sacrificing device stabilities [26–28]. Lewis acid and Lewis base molecules can only passivate one defect type, i.e., negatively charged (electron-rich) and positively charged (electron-poor) defects, respectively [29]. Therefore, a new additive that can efficiently passivate the trap defects and simultaneously improve the long-term stability of PSCs is highly desired [30–36]. Cesium stearate (CsSt) is the Cs source precursor for the preparation of $CsPbBr_3$ quantum dots (QDs) to enable efficient light-emitting diodes, where stearate is beneficial to obtaining the superior crystallinity and stability of QDs due to its characteristics of an anionic surfactant [37–39]. However, currently, a deep understanding of the effect of CsSt on the performance of PSCs is lacking.

Here, we introduce a trace amount of anionic surfactant CsSt into a perovskite precursor solution as grain and interface modifiers. Cesium cation in CsSt is expected to passivate negatively charged defects, and stearate anion in CsSt consisting of a polar carboxylate group and non-polar long-chain alkyl is expected to passivate positively charged defects and tailor the crystallization process. CsSt is proven to enhance the crystallinity of perovskite films, passivate trap defects, and improve the tolerance to light and moisture stress. These augmented film properties allow us to fabricate planar p-i-n structured PSCs with a maximum PCE of 23.41%. The device maintains 91.6% of the initial efficiency after aging in ambient air under AM1.5G solar light (100 mW per cm^2) for 720 h.

EXPERIMENTAL SECTION

Materials

All the chemicals were used as received. Poly(triaryl amine) (PTAA) was purchased from Xi'an Polymer Light Technology

[1] State Key Laboratory of Metal Matrix Composites, Shanghai Jiao Tong University, Shanghai 200240, China
[2] Center of Hydrogen Science, School of Materials Science and Engineering, Shanghai Jiao Tong University, Shanghai 200240, China
[3] Zhangjiang Institute for Advanced Study, Shanghai Jiao Tong University, Shanghai 201210, China
[4] School of Physics, Sydney Nano Institute, The University of Sydney, Sydney NSW 2006, Australia
* Corresponding author (email: yang.xudong@sjtu.edu.cn)

Corp. Lead iodide (PbI_2, 99.99% trace metals basis) and organic halide salts were purchased from Tokyo Chemical Industry. Lead bromide ($PbBr_2$, 99.999% trace metal basis) and cesium iodide (CsI) were purchased from Sigma Aldrich. CsSt was purchased from Xiya Chemical Technology Co., Ltd. Phenyl-C_{61}butyric acid methyl ester (PCBM) and bathocuproine (BCP) were purchased from Luminescence Technology Corp. All the anhydrous solvents were purchased from Sigma-Aldrich.

Perovskite film preparation and device fabrication

Indium tin oxide (ITO)-coated substrates were etched with zinc powder and diluted hydrochloric acid (HCl) to produce desired patterns. The patterned substrates were sequentially cleaned with soap, deionized water, ethanol, and acetone under ultrasonication and then dried with dry nitrogen. Before use, the substrates were cleaned with ultraviolet ozone for 15 min and transferred to an N_2 glove box. The PTAA solution (2 mg mL^{-1}, dissolved in toluene) was spin-coated onto the ITO substrates at a speed of 6000 r min^{-1} for 35 s, and then the films were annealed at 100°C for 10 min. The perovskite films were fabricated by the anti-solvent method. The $(CsPbI_3)_{0.05}[(FAPbI_3)_{0.95}(MAPbBr_3)_{0.05}]_{0.95}$ perovskite solution (1.4 mol L^{-1}, *N*,*N*-dimethylformamide (DMF)/dimethyl sulfoxide (DMSO) = 4:1) with or without a trace amount (0.1 wt%) of CsSt was spin-coated at 2000 r min^{-1} for 10 s and 4000 r min^{-1} for 30 s onto the ITO/PTAA substrates. During the spin-coating, 150 μL of ethyl acetate was poured on the center of the spinning substrates after spinning for 30 s; the samples were then heated at 100°C for 30 min. PCBM (20 mg L^{-1} in chlorobenzene) was spun onto the perovskite layer at a speed of 1000 r min^{-1}. The BCP-saturated solution (150 μL) in methanol was dropped onto the samples drop by drop at 5000 r min^{-1}. Finally, the samples were transferred to an evaporation chamber, and silver (80 nm) was deposited under a vacuum (<10^{-5} Pa).

Characterizations

The top-view scanning electron microscopy (SEM) images were acquired *via* field emission SEM (JSM-7800F, JEOL). The X-ray diffraction (XRD) patterns were recorded on a Rigaku Ultima IV powder X-ray diffractometer using Cu Kα radiation. Ultraviolet-visible (UV-vis) absorption spectra of the perovskite film samples were recorded by a Shimadzu UV 2450 spectrometer. Steady-state photoluminescence (PL) spectra and time-resolved PL (TRPL) spectra were obtained by the FLS1000 spectrometer. The sample configurations of quartz glass/perovskite were used to assess the perovskite film quality, and those of quartz glass/perovskite/PCBM were used to assess the charge transport between the perovskite layers and electron transporting layers (ETLs). The excitation and collection of the PL and TRPL spectra were from the glass side of the samples. The excitation wavelength was set as 520 nm. The ultraviolet photoelectron spectroscopy (UPS) was measured using Thermo ESCALAB 250 with a non-monochromated He Iα photon source ($h\nu$ = 21.22 eV). Atomic force microscopy (AFM) and Kelvin probe force microscopy (KPFM) were recorded by a Bruker FastScan Bio instrument. The contact potential difference (CPD) can be calculated using the following equation: CPD = ($\Phi_{sample} - \Phi_{tip}$) / e, where Φ_{sample} and Φ_{tip} are the work functions of the sample surface and Pt/Ir-coated tip, respectively, and e is the elementary charge of an electron. Φ_{tip} was calibrated with Au (5.2 eV). The static contact angle with the water droplet was measured on a DSA 100 contact angle measuring device (KRUSS GmbH, Germany). The confocal PL mapping images were carried out on a Leica TCS SP8 STED 3X system. The excitation wavelength was set at 470 nm, and the detection range was 700–800 nm. The trap density of the perovskite films was determined by the space-charge-limited current (SCLC) method on the hole-only device with the architecture of the ITO/PTAA/perovskite/Spiro-OMeTAD/Ag. The trap-filled limit voltage (V_{TFL}) determined as the onset voltage of the TFL regime (n > 3) can be used to calculate N_t with the equation: $N_t = 2\varepsilon_0\varepsilon_r V_{TFL} / qL^2$, in which ε_0 is the vacuum permittivity, ε_r is the relative permittivity of perovskite, which can be taken as the value of 46.9 for $FAPbI_3$, q is the elementary charge, and L is the thickness of the perovskite film [40].

Field emission SEM (TESCAN MAIA3 GMU model 2016) was used to observe the cross-sectional SEM image of the complete device. The current-voltage (*I*-*V*) curves of the PSCs were measured with a digital source meter (Keithley 2400) under simulated solar illumination at AM1.5G (100 mW cm^{-2}). The light source was calibrated by a standard silicon reference cell (Wacom Denso Co., Japan). The measurement was conducted with forward (from −0.2 to 1.2 V) scan. The step voltage and delay time were fixed at 10 mV and 200 ms, respecttively. Incident photo-to-electron conversion efficiency spectum measurements were characterized using monochromatic incident light of 1×10^{16} photons cm^{-2} with the alternating current mode. All the tested cells in photovoltaic measurements were covered with a 0.08 cm^2 shading mask. The moisture stability test was conducted without encapsulation. The devices were placed in the air. The relative humidity in the laboratory was around 50% during the entire aging test.

RESULTS AND DISCUSSION

Structural and optical properties of the CsSt-treated perovskites

A trace amount of CsSt (0.1 wt%) was directly added to the perovskite precursor to prepare perovskite thin films through the conventional antisolvent method. The CsSt molecule has a hydrophobic long alkyl chain and carboxyl group that anchors to the X-site of perovskites. The anionic surfactant nature of CsSt is expected to control the crystallization of perovskite films. The XRD patterns (Fig. 1a) of the pristine and CsSt-modified perovskite films were determined to assess the effect of CsSt on the perovskite crystallinity. The (100) diffraction peak at 14.0° of the CsSt-modified perovskite film shows a higher intensity and narrower full width at half maximum than that of the pristine film (Table S1), indicating that CsSt can improve the crystallinity of perovskite films. Moreover, the ratio of the (100) plane to the other crystal planes ((110), (111), (210), and (211)) in the perovskite films was significantly increased after adding CsSt, facilitating a charge transport in the vertical direction [41]. This observation indicates that the anionic surfactant CsSt anchored to perovskites can regulate the growth rates of different crystal planes and eventually promote the formation of films dominated by the (100) orientation. The top-view SEM images in Fig. 1b, c and Fig. S1 show that the perovskite films without and with CsSt have similar grain sizes. The CsSt-modified perovskite grains show more pronounced steps, indicating an enhanced crystallinity [42]. The AFM was further detected to study the effect of CsSt on the surface features of perovskite films (Fig. S2). The CsSt-modified perovskite film shows a smoother surface with a

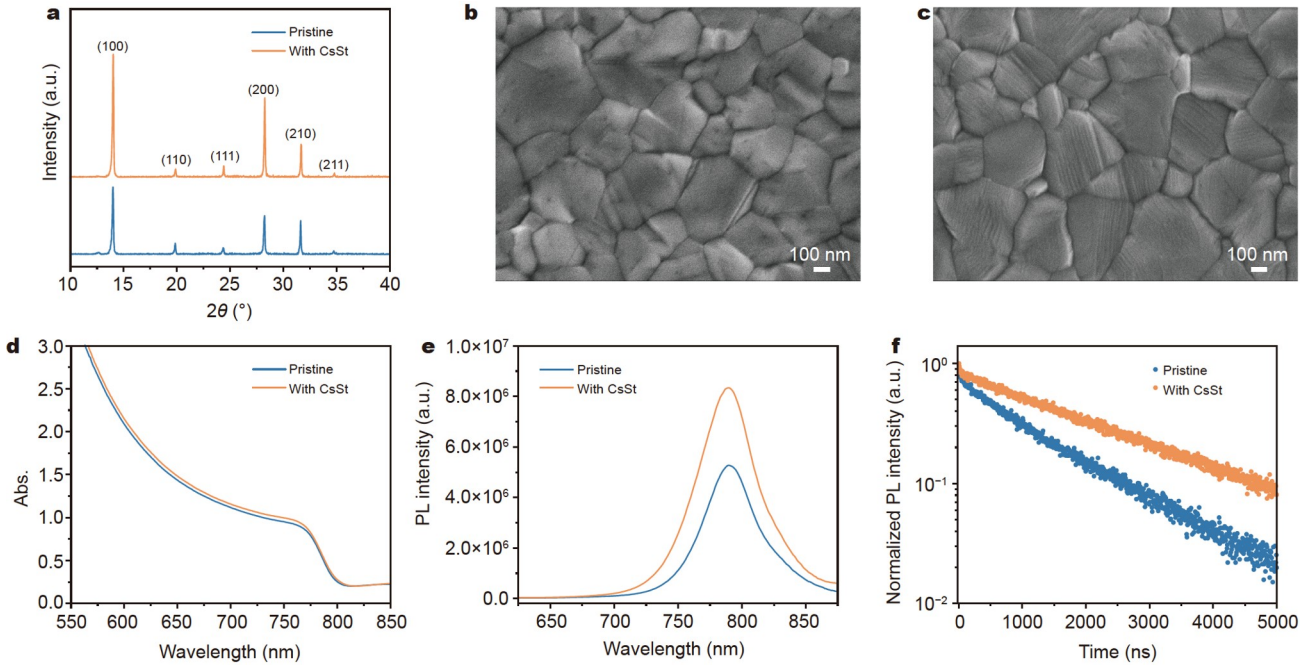

Figure 1 Structural and optical characterization of the perovskite films. (a) XRD patterns of perovskite films without and with CsSt. Top-view SEM images of the (b) pristine perovskite film and (c) perovskite film with CsSt, respectively. (d) Optical absorbance spectra, (e) steady PL spectra, and (f) TRPL decay profiles of perovskite films without and with CsSt.

lower roughness parameter (R_q = 16.0 nm) compared with the pristine perovskite film (R_q = 22.7 nm), which benefits the contact between the perovskite layer and ETLs [11]. In Fig. 1d, the light absorption of the perovskite film is enhanced after CsSt modification due to the improved crystallinity. The Tauc plots from the optical absorbance spectra show an optical bandgap of 1.56 eV for our perovskite films (Fig. S3).

We used steady-state PL and TRPL spectroscopy to assess the perovskite film quality after CsSt modification. As shown in Fig. 1e, the steady PL spectra show that the CsSt-modified perovskite film presents a high emission intensity at ~790 nm, indicating a good quality of the perovskite crystal with a low density of trap states. The TRPL decays were fitted by bi-exponential components using the equation [$Y = A_1\exp(-t / \tau_1) + A_2\exp(-t / \tau_2)$], where the fast decay lifetime τ_1 and slow decay lifetime τ_2 are related to the trap-assisted nonradiative and radiative recombinations, respectively (Table S2) [43]. In Fig. 1f, the PL lifetimes of the perovskite film with CsSt (109 and 1948 ns) are much longer than those of the pristine film (60 and 1253 ns). This finding further confirms that the nonradiative carrier recombination was effectively suppressed by the anionic surfactant CsSt. We infer that CsSt can effectively passivate negatively and positively charged defects, and the thin CsSt insulating layer assembled on the surfaces and grain boundaries acts as a quantum tunneling layer to suppress nonradiative charge-carrier recombination. We further monitored the confocal PL mappings of the perovskite films without and with CsSt under the same excitation conditions (Fig. S4), and enhanced luminescent properties were observed in the CsSt-modified film. The SCLC measurement was conducted to characterize the trap density of perovskite films after CsSt modification (Fig. S5). The calculated hole trap state density decreased from 1.504×10^{15} to 1.190×10^{15} cm^{-3}, indicating that CsSt efficiently passivates charged defects at the surfaces and grain boundaries [44].

Electronic structure of CsSt-treated perovskites

The remarkable improvement in the film quality prompted us to investigate the effect of CsSt on electronic properties. We performed UPS measurements to obtain the detailed electronic structures of the pristine and CsSt-modified perovskite films (Fig. 2a, b). The Fermi level (E_F) deduced from the high-binding-energy cutoff in Fig. 2a upshifted from −4.61 to −4.43 eV after introducing CsSt. The valence band maximums of the pristine film and CsSt-modified film were located at 1.08 and 1.31 eV below E_F, respectively (Fig. 2b). The energy-level diagrams of the perovskite films and carrier transporting layers are depicted in Fig. 2c. The CsSt-modified perovskite film shows a more n-type nature because its E_F is closer to the conduction band minimum, which is likely attributed to the passivated electron traps at surfaces and crystal boundaries [16,45]. We infer that the carboxyl group of CsSt can bond with the uncoordinated Pb at crystal boundaries, resulting in a large fraction of occupied vacant traps [11]. Moreover, this optimized electronic structure after CsSt modification can smoothen the band barriers between the perovskite layers and ETLs and enable efficient carrier separation and transportation at the electron-selective interfaces [46]. We also confirmed the shallower work function of the CsSt-modified perovskite film by KPFM, as shown in Fig. 2d, e. To assess the charge transport between the perovskite layers and ETLs, we conducted the TRPL spectroscopy for the perovskite films with PCBM quenching (Fig. 2f). The quenched carrier times (τ_1, τ_2) were (58 ns, 185 ns) and (26 ns, 157 ns) for the pristine and CsSt-modified films, respectively (Table S3). This observation confirms that the CsSt modification promotes the charge transfer at the electron-selective interfaces.

Photovoltaic performance of the CsSt-treated perovskites

To evaluate the effect of CsSt modification on the photovoltaic

performance of the planar p-i-n structured PSCs, we fabricated the PSCs with the configuration of glass/ITO/PTAA/CsSt-modified perovskite/PCBM/BCP/Ag. The cross-sectional SEM image in Fig. 3a shows a 560-nm-thick perovskite absorber layer with highly crystalline grains, where the grain sizes are greater than the thickness of the film. We fine-tuned the concentration

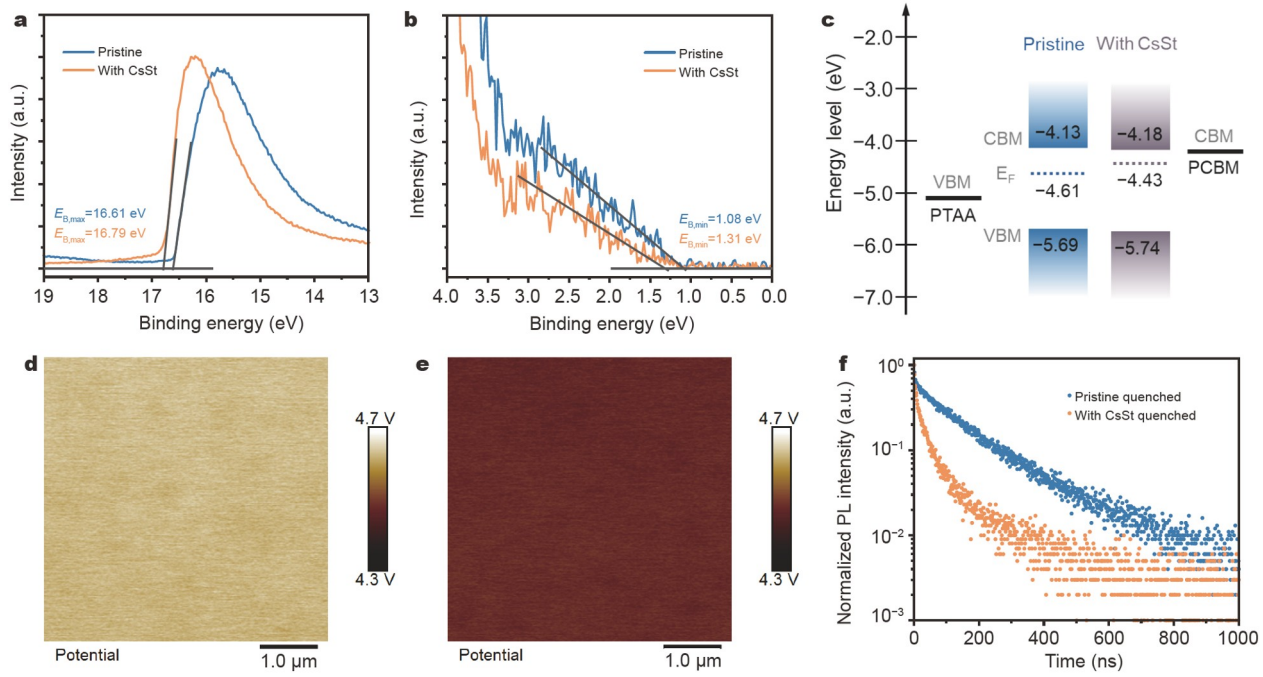

Figure 2 Energy-level characterization of perovskite films after CsSt modification. (a) High-binding-energy and (b) low-binding-energy cutoffs in the UPS spectra of the perovskite films without and with CsSt. (c) Energy-level diagrams for the perovskite layers and carrier transporting layers. *XY*-plane work function mapping images of the (d) pristine perovskite film and (e) perovskite film with CsSt. The mean work function values of the pristine and CsSt-modified perovskite films are 4.59 and 4.46 eV, respectively. (f) TRPL decay profiles of the quenched perovskite samples without and with CsSt, fabricated by spin coating the PCBM solution on the surface of the perovskite films.

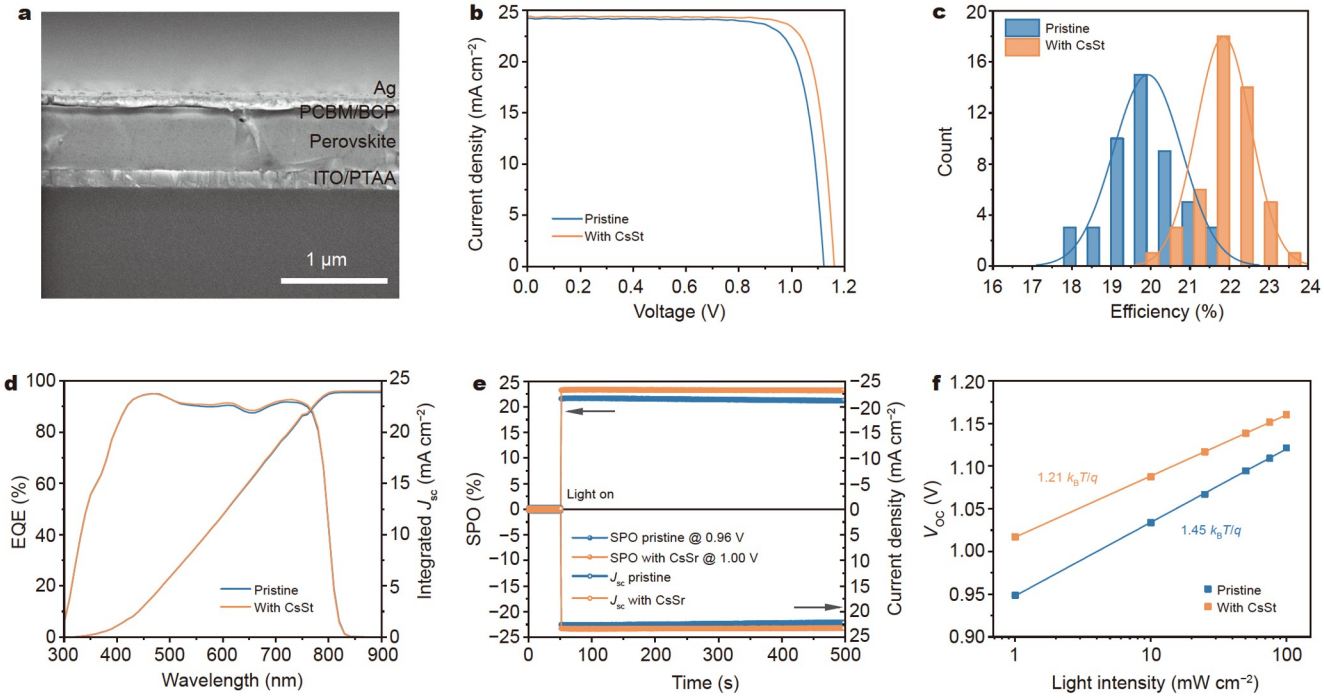

Figure 3 Photovoltaic performance of the PSCs after the CsSt modification. (a) Cross-sectional SEM images of the p-i-n structured PSCs with CsSt. (b) *J-V* characteristics of the best-performing PSCs without and with CsSt. (c) Distribution of the PCEs of the devices. (d) EQE curves and integrated J_{SC} of the best-performing devices. (e) Stabilized power output and photocurrent of the champion devices without and with CsSt at MPP voltages of 0.96 and 1.00 V, respectively. (f) Light intensity-dependent V_{OC} for the devices.

of CsSt from 0.05 to 0.2 wt%, and the optimal performance was found at a concentration of 0.1 wt% (Fig. S6). Fig. 3b shows the current density (J)-voltage (V) characteristics of the best-performing devices without and with CsSt. The control device without CsSt shows a maximum PCE of 21.82%, with a short-circuit current density (J_{SC}) of 24.23 mA cm^{-2}, an open-circuit voltage (V_{OC}) of 1.122 V, and a fill factor (FF) of 80.24% (Table S4). After the CsSt introduction, the best target device exhibited a significantly improved performance with a PCE of 23.41%, J_{SC} of 24.45 mA cm^{-2}, V_{OC} of 1.161 V, and FF of 82.42%. We ascribe the performance enhancement to the improved film crystallinity and efficient passivation of the trap states in the CsSt-modified perovskite films. The histogram of the measured PCEs shows that the average PCE increased from 19.93% to 21.92% after the CsSt modification (Fig. 3c), indicating a dramatic reproducibility of the photovoltaic performance improvement with CsSt. In Fig. S7, the lower PCE of the stearic acid-modified PSC compared with the CsSt-modified PSC indicates that cesium cations and stearate anions contribute to passivating different types of defects [11,47]. In Fig. 3d, the higher external quantum efficiency (EQE) at the absorption region of 600–800 nm was mainly attributed to the improved perovskite crystallinity with CsSt. The integrated J_{SC} of the pristine and CsSt-modified PSCs were 23.87 and 24.01 mA cm^{-2}, respectively, which are consistent with the measured J_{SC} under the solar simulator. The stabilized PCE of the CsSt-modified PSC under maximum power point (MPP) tracking reached 23.3%, which is larger than the value of 21.6% for the pristine device mainly due to the increased V_{OC} (Fig. 3e). We also measured the light-intensity-dependent V_{OC}, as shown in Fig. 3f. The ideality factor (η_{id}) was deduced from the slope described by $\eta_{id}k_BT/q$, where k_B is the Boltzmann constant, T is the temperature, and q is the electron charge [48]. The CsSt-modified device shows an η_{id} of 1.21, closer to 1 compared with 1.45 of the pristine device. This result is attributed to the effectively suppressed trap-assisted nonradiative recombination by the CsSt modification, contributing to the enhanced V_{OC}.

Impact of CsSt on the ambient stability

We measured the water contact angles to evaluate the wettability

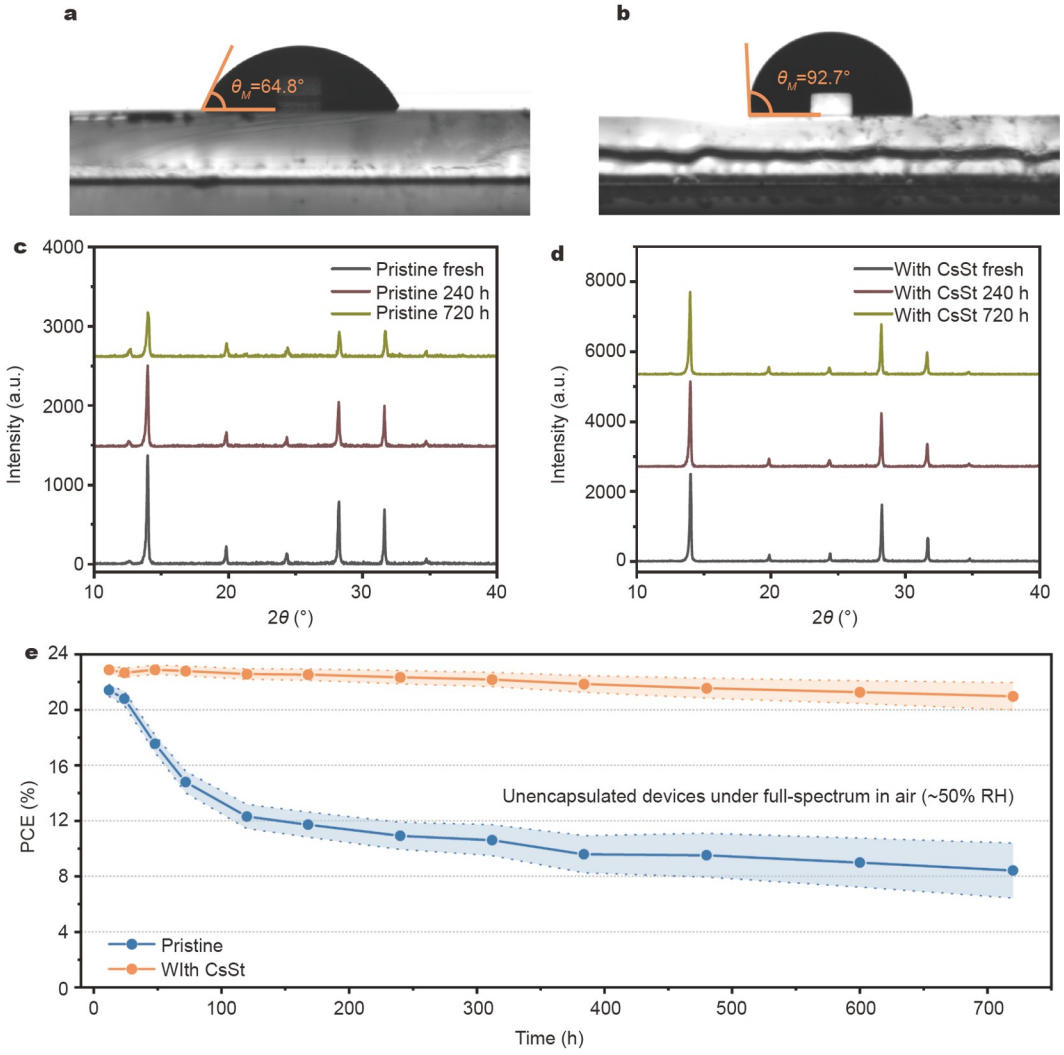

Figure 4 Hydrophobicity and long-term stability. Water contact angle measurements of the (a) pristine and (b) CsSt-modified perovskite films. XRD patterns of the (c) pristine and (d) CsSt-modified perovskite films after being aged under standard light with a humidity of around 50% RH. (e) Long-term ambient stability of the unencapsulated devices without and with CsSt under simulated AM1.5 G radiation (100 mW cm^{-2}) in the air (~50% RH). The shaded regions represent standard deviations from the average PCEs obtained from eight aged devices.

properties of the perovskite films after the CsSt introduction (Fig. 4a, b). The water contact angle for the pristine perovskite film was 60°, and it dramatically increased to 92.7° for the film with CsSt. This observation suggests that CsSt molecules with long alkyl chains can assemble on the perovskite surface, thus significantly enhancing the hydrophobicity of the perovskite films, as shown in Fig. S8. In addition, the carboxyl group of CsSt anchoring to perovskites passivates the X-site defects, and Cs^+ passivates the A-site defects [23]. The XRD patterns of the aged perovskite films in Fig. 4c, d demonstrate that CsSt provided additional protection for perovskites under light and moisture stress. We finally monitored the long-term stability of the non-encapsulated PCSs in wet conditions (~50% relative humidity (RH)) under simulated AM1.5 G radiation (100 mW cm^{-2}) (Fig. 4e). The pristine PSC lost 60.7% of its initial PCE after aging for 720 h, whereas the CsSt-modified device still maintained the value of 91.6% over the same aging period and retained a PCE of 20.98%. The improvement of the ambient stability benefited from the assembled moisture barrier at the perovskite surface and reduced defects at surfaces and grain boundaries.

CONCLUSIONS

The introduction of anionic surfactant CsSt improved the optoelectronic properties by promoting a preferential crystallization orientation and suppressing trap states. Our strategy also enhanced the PCE of p-i-n structured devices up to 23.41% and dramatically improved the ambient stability. Further understanding of the synergistic role of anionic surfactants in polycrystalline perovskite films will provide a new pathway for future photovoltaic devices with superior performance and stability.

Received 8 June 2022; accepted 14 September 2022; published online 14 October 2022

1 National Renewable Energy Laboratory (NREL). Best research-cell efficiency chart (2022). www.nrel.gov/pv/cell-efficiency.html
2 Green MA, Dunlop ED, Hohl-Ebinger J, *et al.* Solar cell efficiency tables (Version 58). Prog Photovolt Res Appl, 2021, 29: 657–667
3 Chang NL, Yi Ho-Baillie AW, Basore PA, *et al.* A manufacturing cost estimation method with uncertainty analysis and its application to perovskite on glass photovoltaic modules. Prog Photovolt-Res Appl, 2017, 25: 390–405
4 Chen H, Teale S, Chen B, *et al.* Quantum-size-tuned heterostructures enable efficient and stable inverted perovskite solar cells. Nat Photon, 2022, 16: 352–358
5 Azmi R, Ugur E, Seitkhan A, *et al.* Damp heat-stable perovskite solar cells with tailored-dimensionality 2D/3D heterojunctions. Science, 2022, 376: 73–77
6 Li X, Zhang W, Guo X, *et al.* Constructing heterojunctions by surface sulfidation for efficient inverted perovskite solar cells. Science, 2022, 375: 434–437
7 Li Z, Li B, Wu X, *et al.* Organometallic-functionalized interfaces for highly efficient inverted perovskite solar cells. Science, 2022, 376: 416–420
8 Luo D, Su R, Zhang W, *et al.* Minimizing non-radiative recombination losses in perovskite solar cells. Nat Rev Mater, 2020, 5: 44–60
9 Cheng Y, Ding L. Pushing commercialization of perovskite solar cells by improving their intrinsic stability. Energy Environ Sci, 2021, 14: 3233–3255
10 Wolff CM, Caprioglio P, Stolterfoht M, *et al.* Nonradiative recombination in perovskite solar cells: The role of interfaces. Adv Mater, 2019, 31: 1902762
11 Zhu L, Zhang X, Li M, *et al.* Trap state passivation by rational ligand molecule engineering toward efficient and stable perovskite solar cells exceeding 23% efficiency. Adv Energy Mater, 2021, 11: 2100529
12 Li N, Niu X, Chen Q, *et al.* Towards commercialization: the operational stability of perovskite solar cells. Chem Soc Rev, 2020, 49: 8235–8286
13 Zheng G, Zhu C, Ma J, *et al.* Manipulation of facet orientation in hybrid perovskite polycrystalline films by cation cascade. Nat Commun, 2018, 9: 2793
14 Bu T, Liu X, Zhou Y, *et al.* A novel quadruple-cation absorber for universal hysteresis elimination for high efficiency and stable perovskite solar cells. Energy Environ Sci, 2017, 10: 2509–2515
15 Saliba M, Matsui T, Domanski K, *et al.* Incorporation of rubidium cations into perovskite solar cells improves photovoltaic performance. Science, 2016, 354: 206–209
16 Zheng X, Hou Y, Bao C, *et al.* Managing grains and interfaces *via* ligand anchoring enables 22.3%-efficiency inverted perovskite solar cells. Nat Energy, 2020, 5: 131–140
17 Jung M, Shin TJ, Seo J, *et al.* Structural features and their functions in surfactant-armoured methylammonium lead iodide perovskites for highly efficient and stable solar cells. Energy Environ Sci, 2018, 11: 2188–2197
18 Lee JW, Dai Z, Han TH, *et al.* 2D perovskite stabilized phase-pure formamidinium perovskite solar cells. Nat Commun, 2018, 9: 3021
19 Lee JW, Tan S, Seok SI, *et al.* Rethinking the A cation in halide perovskites. Science, 2022, 375: eabj1186
20 Shao Y, Xiao Z, Bi C, *et al.* Origin and elimination of photocurrent hysteresis by fullerene passivation in $CH_3NH_3PbI_3$ planar heterojunction solar cells. Nat Commun, 2014, 5: 5784
21 Xu J, Buin A, Ip AH, *et al.* Perovskite-fullerene hybrid materials suppress hysteresis in planar diodes. Nat Commun, 2015, 6: 7081
22 Wang K, Liu C, Du P, *et al.* Bulk heterojunction perovskite hybrid solar cells with large fill factor. Energy Environ Sci, 2015, 8: 1245–1255
23 Wang R, Xue J, Meng L, *et al.* Caffeine improves the performance and thermal stability of perovskite solar cells. Joule, 2019, 3: 1464–1477
24 Lee JW, Bae SH, Hsieh YT, *et al.* A bifunctional Lewis base additive for microscopic homogeneity in perovskite solar cells. Chem, 2017, 3: 290–302
25 Liu X, Wu J, Yang Y, *et al.* Pyridine solvent engineering for high quality anion-cation-mixed hybrid and high performance of perovskite solar cells. J Power Sources, 2018, 399: 144–150
26 Lee DG, Kim DH, Lee JM, *et al.* High efficiency perovskite solar cells exceeding 22% *via* a photo-assisted two-step sequential deposition. Adv Funct Mater, 2021, 31: 2006718
27 Boyd CC, Cheacharoen R, Leijtens T, *et al.* Understanding degradation mechanisms and improving stability of perovskite photovoltaics. Chem Rev, 2019, 119: 3418–3451
28 Eames C, Frost JM, Barnes PRF, *et al.* Ionic transport in hybrid lead iodide perovskite solar cells. Nat Commun, 2015, 6: 7497
29 Wang J, Jin G, Zhen Q, *et al.* Bulk passivation and interfacial passivation for perovskite solar cells: Which one is more effective? Adv Mater Interfaces, 2021, 8: 2002078
30 Qin C, Matsushima T, Fujihara T, *et al.* Multifunctional benzoquinone additive for efficient and stable planar perovskite solar cells. Adv Mater, 2017, 29: 1603808
31 Cai Y, Cui J, Chen M, *et al.* Multifunctional enhancement for highly stable and efficient perovskite solar cells. Adv Funct Mater, 2021, 31: 2005776
32 Shi X, Wu Y, Chen J, *et al.* Thermally stable perovskite solar cells with efficiency over 21% *via* a bifunctional additive. J Mater Chem A, 2020, 8: 7205–7213
33 Yang Y, Peng H, Liu C, *et al.* Bi-functional additive engineering for high-performance perovskite solar cells with reduced trap density. J Mater Chem A, 2019, 7: 6450–6458
34 Li Z, Li X, Wang M, *et al.* Enhanced photovoltaic performance *via* a bifunctional additive in tin-based perovskite solar cells. ACS Appl Energy Mater, 2022, 5: 108–115
35 Mateen M, Arain Z, Liu X, *et al.* Boosting optoelectronic performance of $MAPbI_3$ perovskite solar cells *via* ethylammonium chloride additive engineering. Sci China Mater, 2020, 63: 2477–2486
36 Wu G, Cai M, Cao Y, *et al.* Enlarging grain sizes for efficient perovskite solar cells by methylamine chloride assisted recrystallization. J Energy

Chem, 2022, 65: 55–61
37 Song J, Li J, Li X, *et al.* Quantum dot light-emitting diodes based on inorganic perovskite cesium lead halides ($CsPbX_3$). Adv Mater, 2015, 27: 7162–7167
38 Li J, Xu L, Wang T, *et al.* 50-Fold EQE improvement up to 6.27% of solution-processed all-inorganic perovskite $CsPbBr_3$ QLEDs *via* surface ligand density control. Adv Mater, 2017, 29: 1603885
39 Li Y, Ma F, Zhao D, *et al.* Convenient synthesis of high-quality, all-inorganic lead halide perovskite nanocrystals for high purity monochrome QLED. Mater Tech, 2021, 36: 637–646
40 Chen Y, Yang Z, Wang S, *et al.* Design of an inorganic mesoporous hole-transporting layer for highly efficient and stable inverted perovskite solar cells. Adv Mater, 2018, 30: 1805660
41 Kim H, Lee YH, Lyu T, *et al.* Boosting the performance and stability of quasi-two-dimensional tin-based perovskite solar cells using the formamidinium thiocyanate additive. J Mater Chem A, 2018, 6: 18173–18182
42 Singh CR, Gupta G, Lohwasser R, *et al.* Correlation of charge transport with structural order in highly ordered melt-crystallized poly(3-hexylthiophene) thin films. J Polym Sci Part B-Polym Phys, 2013, 51: 943–951
43 Jeong M, Choi IW, Go EM, *et al.* Stable perovskite solar cells with efficiency exceeding 24.8% and 0.3-V voltage loss. Science, 2020, 369: 1615–1620
44 Liu K, Liang Q, Qin M, *et al.* Zwitterionic-surfactant-assisted room-temperature coating of efficient perovskite solar cells. Joule, 2020, 4: 2404–2425
45 Yang X, Fu Y, Su R, *et al.* Superior carrier lifetimes exceeding 6 μs in polycrystalline halide perovskites. Adv Mater, 2020, 32: 2002585
46 Quarti C, De Angelis F, Beljonne D. Influence of surface termination on the energy level alignment at the $CH_3NH_3PbI_3$ perovskite/C60 interface. Chem Mater, 2017, 29: 958–968
47 Li B, Chang B, Pan L, *et al.* Tin-based defects and passivation strategies in tin-related perovskite solar cells. ACS Energy Lett, 2020, 5: 3752–3772
48 Kim M, Jeong J, Lu H, *et al.* Conformal quantum dot-SnO_2 layers as electron transporters for efficient perovskite solar cells. Science, 2022, 375: 302–306

Acknowledgements This work was supported by the National Key Research and Development Program of China (2018YFB1500104), the National Natural Science Foundation of China (11574199 and 11911530142), Shanghai Pilot Program for Basic Research-Shanghai Jiao Tong University, and the Program for Professor of Special Appointment (Eastern Scholar) at Shanghai Institutions of Higher Learning. We gratefully acknowledge the assistance in measurements from the Instrumental Analysis Center of Shanghai Jiao Tong University (China). We especially thank Li H for the assistance with the AFM and KPFM measurements, Bao Z and Li X for the assistance with the SEM measurements, and Wang R for the assistance with the PL and TRPL measurements. We thank Han L for the helpful discussions.

Author contributions Yang X supervised the project. Yang X and Wang T conceived the ideas for the project and designed the experiments. Wang T, Ye T, Qiao L, and Kong W characterized the films and devices. Wang T, Ye T, Qiao L, Kong W, Zeng F, Zhang Y, Sun R, and Zhang L optimized the photovoltaic performance of devices together. Chen H and Zheng R participated in the discussion and revision. Yang X and Wang T co-wrote the manuscript.

Conflict of interest The authors declare that they have no conflict of interest.

Supplementary information Supporting data are available in the online version of the paper.

Tao Wang is currently a PhD candidate at the School of Materials Science and Engineering, Shanghai Jiao Tong University. He received his MS degree from the School of Chemistry and Chemical Engineering, Nanjing University in 2018. His current research is focused on fabricating highly efficient and stable perovskite solar cells through addictive engineering, interface engineering, and doping strategies for organic hole-transporting materials.

Xudong Yang received his PhD degree from the Chinese Academy of Sciences. He did postdoctoral research at the University of Cambridge, UK, and the International Center for Young Scientists of the National Institute for Materials Science, Japan. He joined Shanghai Jiao Tong University as a distinguished researcher in 2014. His current research is focused on understanding the mechanisms of photoelectron conversion, charge transport, and the fabrication of next-generation optoelectronic devices for applications in energy conversion.

阴离子表面活性剂锚定实现23.4%转换效率的反式钙钛矿太阳能电池

王涛[1,2,3], 叶天时[1,2,3], 乔亮[1,2,3], 孔维瑜[1,2,3], 曾芳[4], 张尧[1], 孙瑞田[1,2,3], 张林[1,2,3], 陈汉[1], 郑荣坤[4], 杨旭东[1,2,3*]

摘要 金属卤化物钙钛矿薄膜缺陷处的非辐射复合损失仍然是阻碍钙钛矿太阳能电池光伏性能和稳定性进一步提高的主要原因. 本文中, 我们报道了一种可行的多功能添加剂策略, 通过使用硬脂酸铯来钝化钙钛矿薄膜中的缺陷, 同时提高对光和湿度的耐受性. 实验证明, 目标薄膜中的非辐射复合损失得到了有效抑制, 同时硬脂酸铯提高了薄膜结晶度, 降低了陷阱态密度, 增强了界面载流子的分离和传输. 因此, 本策略将p-i-n反式结构钙钛矿太阳能电池的功率转换效率提高到23.41%. 该器件在没有封装的情况下以及潮湿空气中表现出良好的长期稳定性, 在720 h后仍能保持初始效率的91.6%.

